Two zone transient storage modeling using temperature and solute data with multiobjective calibration: Part 1 Temperature

B. T. Neilson[a], D. K. Stevens[b], S.C. Chapra[c], C. Bandaragoda[d]

[a]Utah State University, Civil and Environmental Engineering, Utah Water Research Laboratory, 8200 Old Main Hill, Logan, UT 84321, USA, bethany.neilson@usu.edu, 435-797-7369

[b] Utah State University, Civil and Environmental Engineering, Utah Water Research Laboratory, 8200 Old Main Hill, Logan, UT 84321, USA, david.stevens@usu.edu, 435-797-3229

[c]Tufts University, Civil and Environmental Engineering, 113 Anderson Hall, Medford, MA 02155, USA, steven.chapra@tufts.edu, 617-627-3654

[d] Silver Tip Solutions, 10623 56th Ave W, Mukilteo, WA, 98275, USA, christina@silvertipsol.com, 425-501-4191

Two zone transient storage modeling using temperature and solute data with multiobjective calibration: Part 1 Temperature

B. T. Neilson, D. K. Stevens, S.C. Chapra, C. Bandaragoda

Abstract

This paper presents the formulation and calibration of the temperature portion of a two-zone temperature and solute (TZTS) model which separates transient storage into surface (STS) and subsurface transient storage (HTS) zones. The inclusion of temperature required the TZTS model formulation to differ somewhat from past transient storage models in order to accommodate terms associated with heat transfer. These include surface heat fluxes in the main channel (MC) and STS, heat and mass exchange between the STS and MC, heat and mass exchange between the HTS and MC, and heat exchange due to bed and deeper ground conduction. To estimate the additional parameters associated with a two-zone model, a data collection effort was conducted to provide temperature time series within each zone. Both single and multi-objective calibration algorithms were then linked to the TZTS model to assist in parameter estimation. Single objective calibrations based on MC temperatures at two different locations along the study reach provided reasonable predictions in the MC and STS. The HTS temperatures were consistently poorly estimated. The two objective calibration using MC temperatures simultaneously at two locations illustrated that the TZTS model accurately predicts

temperatures observed in MC, STS and HTS zones, including those not used in the calibration. These results suggest that multiple data sets representing different characteristics of the system should be used when calibrating complex instream models.

Key words: two-zone modeling, instream temperature modeling, multi-objective optimization, hyporheic, dead zone

Index terms: (1814) Energy budgets, (0414) Biogeochemical cycles, processes, and modeling, (1878) Water/energy interactions, (1873) Uncertainty assessment

Introduction

Temperature is a critical physical characteristic of an aquatic system because of its relationship with chemical and biological reaction rates, and with aquatic species that are sensitive to temperature. The most common effects of elevated temperatures on fish species include increased parasitism, weight decrease due to increased metabolic rates [*Sauter et al.*, 2001], problems with early life-stage development [*McCullough et al.*, 2001], and at high enough temperatures, death due to heat stress. Physics-based temperature models quantify the relative importance of various heat fluxes to aid in understanding how management of river systems can affect instream temperatures.

Most temperature models for natural waters include surface heat flux terms for net shortwave radiation, atmospheric longwave radiation, water longwave radiation, and sensible (conduction/convection) and latent heat (evaporation/condensation) exchange. Within shallow streams, there are additional heat transfer mechanisms occurring, namely bed conduction, exchange with the hyporheic zone, influences of surface storage (e.g., dead zones), and solar radiation penetration and attenuation in the water column. Various combinations of these have been incorporated into stream temperature models (e.g., TEMP-84/86 [*Beschta and Weatherred*, 1984; 1987], Heat Source [*Boyd and Kasper*, 2003], SNTEMP [*Theurer et al.*, 1984], and River Modeling System (or RQUAL) [*Hauser and Schohl*, 2003]). However, we are unaware of an instream temperature model that includes all of these fluxes.

Transient storage is defined as the combination of the hyporheic storage, dead zones, and other slow moving water relative to the main channel (MC) flow [*Bencala and Walters*, 1983].

Past efforts to model transient storage processes are commonly implemented in the context of an advection-dispersion model of one-dimensional solute transport, including first-order exchange with the storage zone [*Bencala and Walters*, 1983; *Runkel*, 1998]. This type of model requires estimation of parameters that correspond to storage-zone volume and exchange rates. Because these parameters are difficult to measure directly, they are commonly determined empirically with tracer experiment data. Using the notation of Briggs et al. [2009], the stream-tracer approach to modeling solute transport lumps the surface (STS) and subsurface (HTS) transient storage into one zone (a one-zone stream solute model) and, therefore, the results do not fully distinguish between characteristics of surface and subsurface processes [*Briggs et al.*, 2009; *Harvey and Wagner*, 2000; *Neilson et al.*, 2009; *Packman and Bencala*, 2000; *Runkel and McKnight*, 2003]. Rather, such models represent an averaging of all the processes.

In the context of understanding heat transfer in streams, the temperature responses in each of these transient storage zones will differ because, unlike the HTS zone, the STS zone is exposed to the atmosphere and direct sunlight [*Neilson*, 2006; *Neilson et al.*, 2009; *Runkel and McKnight*, 2003], therefore, it is important to consider the two zones independently. Neilson et al. [2009] stressed the need to separate these zones by showing that the STS and HTS heat fluxes contribute differently to MC diel fluctuations. While the need for models with multiple storage zones is evident and the mathematical formulation may be straightforward, the development of practical field methods to parameterize such a model may not be as simple [*Runkel and McKnight*, 2003].

Beyond issues associated with collecting data to support parameter estimation, adding complexity to models, such as the addition of storage zones, increases the number of parameters

requiring estimation and demands increasingly robust calibration approaches. Other issues include parameter non-identifiability, where different parameter sets produce practically indistinguishable results [*Harvey and Wagner*, 2000]. Parameter estimation in hydrologic models has dealt with similar problems and has been a topic of research for a number of years, but the application of the algorithms stemming from these efforts to instream models has been limited. Some recent global calibration/optimization algorithms developed for complex hydrology models include the Shuffled Complex Evolution (SCE-UA) algorithm [*Duan et al.*, 1992] and Shuffled Complex Evolution Metropolis (SCEM-UA) algorithm [*Vrugt et al.*, 2003a]. Both the SCE-UA and SCEM-UA base their search on minimizing a single objective function (e.g., root-mean-square error (RMSE), mean absolute error (MSE), bias, Nash-Sutcliffe Efficiency (*NSE*), etc.) or 'goodness-of-fit' measures [*Legates and McCabe*, 1999]. Vrugt et al. [2003b] stated that single objective functions can be inadequate to identify all the important characteristics of the observations. As a consequence they developed the Multi-objective Shuffled Complex Evolution Metropolis (MOSCEM) algorithm [*Vrugt et al.*, 2003b], building on the SCEM-UA global optimization algorithm, but using the concept of Pareto dominance to address multiple objectives. This algorithm has been most commonly applied in the calibration of hydrologic models with many parameters where multiple calibration time series represent unique characteristics of the system [*Gupta et al.*, 1998; *Schoups et al.*, 2005a; *Schoups et al.*, 2005b; *Vrugt et al.*, 2003b].

To address some of the needs associated with capturing the effects of STS and HTS zones on instream temperatures, we have developed a two-zone temperature and conservative solute (TZTS) model. The present paper focuses on the temperature components of our study; a companion paper [*Neilson et al.*, 2010] focuses on the combined use of temperature and solute

data in model calibration. Although a two-zone model is not a new concept [*Briggs et al.*, 2009; *Choi et al.*, 2000; *Harvey et al.*, 1996; *Harvey et al.*, 2005], our modeling approach is unique in simulating both heat and mass transfer simultaneously between the MC and STS and the MC and HTS zones. Further, inclusion of heat and temperature is an important prerequisite for the effective simulation of biological and chemical processes. The overall goals of this paper are to describe the TZTS model formulation, to expand on the past tracer injection methods of estimating the effects of transient storage through use of temperature to inform transient storage parameter estimates; to highlight the utility of collecting multiple data types in different storage locations; and to provide an initial understanding of parameter uncertainty in two-zone modeling applications through use of both single and multi-objective calibrations.

Two-Zone Temperature Model Formulation: Heat Balance Equations

As depicted in Figure 1, the TZTS model longitudinally divides the MC of the stream into a series of control volumes with solute exchanged between volumes via advection and dispersion [*Chapra*, 1997; *Martin and McCutcheon*, 1999] with the advection process formulated using a kinematic-wave approach [*Chapra*, 1997]. Each volume is also connected via mass transfer with two storage zones that are assumed to be well-mixed : (1) a STS or "dead" zone representing stagnant areas along the stream edge; and, (2) a HTS zone representing a hyporheic region in the stream bed. Sources and sinks of heat include fluxes across the air-water interface (J_{an}, J_{sn}, J_{br}, J_e, and J_c), bed conduction (J_{bed}), conduction between the HTS zone and deeper ground substrate (J_{gr}), exchange with the hyporheic transient storage zone (J_{HTS}),

exchange with the surface transient storage or dead zone (J_{STS}), and conduction between the surface transient storage and sediments ($J_{bed,STS}$, $J_{gr,STS}$) (Figure 2). The TZTS model calculates energy and mass balances for the MC, STS, and HTS zones and/or sediments for each reach or control volume. While the model assumes simple, uniform areas over which exchange between the MC and storage zones takes place, it is recognized that the exchange areas and potential discontinuity along the reach vary greatly, thereby emphasizing the need to sample from many surface and subsurface locations to test the model's ability to represent the physical processes at a reach scale.

Model assumptions, many of which are similar to the one-zone transient storage model, [*Bencala and Walters*, 1983; *Kazezyilmaz-Alhan and Medina Jr.*, 2006] include: completely-mixed reaches and storage zones; steady, non-uniform hydraulics; MC advection and dispersion; one-dimensional first-order mass transfer from the HTS and STS zones across an interfacial area with the MC; hyporheic zone width set to the MC width; analogous mass and heat exchange rates; and bed conduction between the MC water column and bed sediments and the STS water column and bed sediments.

Under these assumptions, mass balances can be written for the main channel (*MC*) and its associated surface storage (*STS*), surface storage sediments (*STS,sed*), and hyporheic storage (*HTS*) zones (see App. 1 for derivation),

$$\frac{\partial T_{MC}}{\partial t} = -U_{MC}\frac{\partial T_{MC}}{\partial x} + D\frac{\partial^2 T_{MC}}{\partial x^2} + \frac{J_{atm}}{\rho C_p Y_{MC}} +$$

$$\frac{\alpha_{STS} Y_{STS}}{A_{cs,MC}\beta B_{tot}}(T_{STS} - T_{MC}) + \frac{Q_{HTS}}{V_{MC}}(T_{HTS} - T_{MC}) + \quad (1)$$

$$\frac{\rho_{sed} C_{p,sed}\alpha_{sed}}{\rho C_p Y_{MC} Y_{HTS}}(T_{HTS} - T_{MC})$$

$$\frac{dT_{STS}}{dt} = \frac{J_{atm,STS}}{\rho C_p Y_{STS}} + \frac{\alpha_{STS}}{(\beta B_{tot})^2}(T_{MC} - T_{STS}) + \frac{\rho_{sed} C_{p,sed}\alpha_{sed}}{\rho C_p Y_{STS} Y_{HTS}}(T_{STS,sed} - T_{STS}) \quad (2)$$

$$\frac{dT_{HTS}}{dt} = \frac{Q_{HTS}}{V_{HTS}}(T_{MC} - T_{HTS}) + \frac{\rho_{sed} C_{p,sed}\alpha_{sed}}{\rho C_p Y_{HTS}^{\ 2}}(T_{MC} - T_{HTS}) + \frac{\rho_{sed} C_{p,sed}\alpha_{sed}}{\rho C_p Y_{HTS} Y_{gr}}(T_{gr} - T_{HTS}) \quad (3)$$

$$\frac{dT_{STS,sed}}{dt} = \frac{\rho_{sed} C_{p,sed}\alpha_{sed}}{\rho C_p Y_{HTS}^2}(T_{STS} - T_{STS,sed}) + \frac{\rho_{sed} C_{p,sed}\alpha_{sed}}{\rho C_p Y_{HTS} Y_{gr}}(T_{gr} - T_{STS,sed}) \quad (4)$$

where T = temperature (°C), Q = volumetric flow rate ($m^3 s^{-1}$), V = zone volume (m^3), D = longitudinal dispersion ($m^2 d^{-1}$), Δx = volume length (m), α_{STSi} = exchange between the MC and

the STS (m^2d^{-1}), Q_{HTS} = HTS advective transport coefficient (m^3d^{-1}), $A_{cs,MC}$ = cross-sectional area of the MC (m^2), B_{tot} = total volume width (m), β = the STS fraction of the total channel width, Y = volume depth (m), ρ = density of the water (g cm^{-3}), C_p = specific heat capacity of the water (cal $g^{-1o}C^{-1}$), ρ_{sed} = density of the sediment (g cm^{-3}), $C_{p,sed}$ = heat capacity of the sediment (cal $g^{-1o}C^{-1}$), α_{sed}= coefficient of thermal diffusivity of the sediment, and J_{atm} = atmospheric heat flux (cal cm^{-2} d^{-1}), which is defined as:

$$J_{atm} = J_{sn} + J_{an} - (J_{br} + J_c + J_e) \tag{5}$$

where J_{sn} = net shortwave radiation (0.31 to 2.8 μm) (cal cm^{-2} d^{-1}), J_{an} = atmospheric longwave radiation (5 to 25 μm) (cal cm^{-2} s^{-1}), J_{br} =water longwave radiation (cal cm^{-2} s^{-1}), J_c = conduction and convection (cal cm^{-2} s^{-1}), and J_e =evaporation and condensation (cal cm^{-2} s^{-1}). The formulations for J_{an}, J_{br}, J_c, and J_e are found in Chapra [1997]. The subscripts *STS,sed,* and *gr* specify the sediments below the STS and the deeper ground layer, respectively.

Since Δx is specified, the model has five free parameters associated with the storage zones, $Q_{HTS,i}$, $Y_{HTS,}$ $\alpha_{STS,i}$, $A_{cs,STS}$, β. Heat and mass transfer are treated analogously, so the equations for solute are similar to Eqs. 1-3 and the storage parameters are the same for both solute and temperature. The channel widths (B_{tot}), longitudinal dispersion (D), and Manning's roughness coefficient (n) are also treated the same way in both the solute and temperature equations. The additional parameters necessary to calculate the heat fluxes include the depth of

the ground conduction zone (Y_{gr}) and those associated with bed and ground conduction [sediment density (ρ_{sed}), heat capacity ($C_{p,sed}$), and coefficient of thermal diffusivity (α_{sed})].

The explicit Euler method with upwind differencing [*Chapra*, 1997; *Hoffman*, 2001] was used to solve the governing equations. Although this forward-time, backward-space scheme is simple to implement, it has two primary deficiencies related to stability and accuracy. In particular, for advection-dominated systems, it requires small time steps to maintain stability and can exhibit significant numerical dispersion. Although these deficiencies make it impractical for large-scale dynamic applications, it is adequate for the present study because we are analyzing steady-flow cases and the impact of numerical dispersion on the analysis is greatly simplified. The basis for choosing the time and space steps is to generate numerical dispersion equal to the actual physical dispersion (App. B); therefore, the dispersion terms are dropped from Eqn. 1 and dispersion is held constant during calibration (that is, it is specified rather than estimated).

This model formulation was primarily driven by parameter requirements for predicting temperature. This resulted in additional parameters beyond those commonly found in standard transient storage zone models (e.g., *Bencala and Walters* [1983]). One key requirement was the need to estimate the surface area of the STS explicitly to calculate the surface fluxes associated with this zone. Equations 6 and 7 demonstrate that the TZTS surface and subsurface storage parameters, respectively, can be related to that of Runkel (1998).

$$\alpha_{OTIS} = \frac{\alpha_{STS} Y_{STS}}{\beta B_{tot} A_{cs,MC}} \tag{6}$$

$$\alpha_{OTIS} = \frac{Q_{HTS} Y_{HTS}^{\ 2}}{\Delta x B_{HTS}^{\ 2} A_{cs,MC}} \quad (7)$$

Methods

Site Description and Data Collection

Temperatures in the Virgin River, Utah, have been studied for more than 30 years because of concern over habitat loss of unique native fishes including two endangered fish species: Virgin River Chub (*Gila seminuda*) and woundfin (*Plagopterus argentissimus*). The section of the Virgin River between Hurricane and Washington, near St. George, UT, chosen for the study (Figure 3) has a typical desert climate with hot, dry summers and maximum daily air temperatures greater than 38˚C for the majority of July and August. Of greatest concern is the low flow, summer season when elevated stream temperatures limit fish habitat. Although large amounts of temperature, flow, and turbidity data have been collected in this portion of the Virgin River, these data were collected to help understand how to meet the water demands of the rapidly growing urban population while considering agricultural and fish habitat requirements, and not to quantify energy fluxes. Managing the river flows to mitigate instream temperature extremes has been hampered by an incomplete understanding of the river's dominant heat fluxes.

Figure 3 shows the 18 km long study reach and data collection points. Although there are several inflows along the reach, the return flow from Quail Creek Reservoir (0.12 m^3s^{-1}) is the

largest and significantly reduces instream temperatures. The study reach was selected in part due to the minimal groundwater influence [*Herbert*, 1995] and was divided into two sections on the basis of bed slope and stream substrate distribution identified from a previous mapping effort. Section 1, including the reaches between CS 1 and a part of the river 1.75 km below CS 2, has an average bed slope of 0.0039 and bed substrate consisting of sand (56%), gravel (26%), and cobble (14%). The lower Section 2 has a mean slope of 0.0012 and bed substrate primarily consisting of sand (72%), gravel (15%), and cobble (10%). Due to these differences, each section has the potential to function differently in terms of surface and subsurface transient storage. As described in Neilson et al. [2009] and shown in Figure 3, there were three primary data collection locations within the study reach. Cross Section 1 (CS 1) is the upper boundary of the study reach with substrate consisting of compacted gravel and cobble, filled with sand. Hurricane Bridge (CS 2), 11 km below CS 1, has substrate consisting of loose and mobile sand. The terminus of the study reach, CS 3, 18 km below CS 1, was located above the backwater of the Washington Fields Diversion structure with substrate similar to CS 2. Throughout the study period, the flow was steady and averaged 2.86 cms and 3.15 cms at CS 1 and CS 3, respectively. Information regarding lateral inflow rates and temperatures (most of which were smaller than 0.07 cms) were collected during the study. Additionally, weather information (air temperature, solar radiation, wind speed, and relative humidity) was gathered at CS 1 using a Wireless Vantage Pro (Hayward,CA) weather station to provide the data necessary calculate the atmospheric fluxes.

In order to support parameter estimation associated with this two-zone model, solute tracer and temperature data were collected from the MC, HTS, and STS as discussed in Neilson et al. [2009]. The use of temperature data in model calibration allows for heat to be used as

tracer [*Constantz*, 2008] and provides calibration data to be collected in a relatively cost-effective manner. Zaramella and Packman [2003] and Harvey and Wagner [2000] both state that there are limitations in relying solely on tracer experiments to determine meaningful information about the surface and subsurface processes. While stream-tracer experiments provide information about time scales of storage, it is important to collect complementary information about subsurface processes [*Harvey and Wagner*, 2000]. In the Virgin River study, two data collection efforts (July and September 2005) included 1) tracer experiments resulting in MC and STS concentrations, and 2) simultaneous MC, STS, and HTS zone temperature data. Neilson et al. [2009] provides more detail regarding the temperature data collection effort and results. Temperature data were collected at six locations in the July study and nine locations in the September study at each of the three cross sections (Figure 3) using Hobo® Water Temp ProV1 (Onset Corporation, Bourne, MA) temperature probes with a ±0.2 °C accuracy and resolution of 0.02 °C.

Figure 4 shows the probe placement at each cross section. Probes 1 and 3 measured the temperatures of representative STS near river right and left. Probe 2 measured MC temperatures. Based on recommendations from Silliman and Booth [1993], probes 4 - 6 were buried at approximately 3, 9, and 20 cm to measure the combined effects of exchange with the hyporheic zone and conduction through the stream bed. In a second data collection effort, three additional probes (7 - 9) were placed in the sediment, but were isolated from lateral hyporheic advection by a plastic cylinder open at both ends (~30 cm diameter and 30 cm tall) and installed flush with the bed. These probes were placed to provide independent measures of vertical heat transfer, which was assumed to be primarily due to conduction at locations where local down-welling or upwelling was not significant.

Data and Parameter Relationships

Many of the parameters within the TZTS model cannot be estimated independently and therefore, must be estimated simultaneously through model calibration. The sediment thermal diffusivity (α_{sed}), however, can be estimated individually for the substrate by using a sediment-water heat exchange model if data are collected from the bed sediments that represent only the effects of conduction. In this application, temperatures from probe 2 were used as a boundary condition and the temperatures at different sediment depths (probe 7 - 9 in locations where minimal advection is occurring in the cylinder) were used to estimate the sediment thermal diffusivity (α_{sed}) by inverse modeling [*Chapra*, 2006]. The sediment density (ρ_{sed}) and heat capacity ($C_{p,sed}$) were taken from Chapra et al. [2004].

The data collection effort was designed to provide specific information about the exchange rates by placing temperature probes to measure temperature differences between the main channel and each zone. For example, information regarding exchange rates and volumes for the STS are provided by temperature probes 1 and 3 and for the HTS exchange through the sediment temperature probes 4 – 6. Table 1 provides a list of the data time series and the related parameters as established through a manual sensitivity analysis.

The MC temperatures provide information about many of the key calibration parameters. In this study, we assume that if the MC temperatures are predicted correctly and the other independent measures of the storage zones are captured well (e.g., storage zone solute concentrations and temperatures), the dominant processes within each zone and the interactions

with the MC are being captured within the model at the reach scale. The MC temperature time series also provides information about the total channel width since these temperatures are related to the area over which surface fluxes occur. In this application, the Δx was set to 31.3 m and the Δt was kept at approximately four seconds to mimic physical dispersion (D) (Appendix 2). Therefore, D was not estimated during the calibration and is not included in Table 2. The utility of the tracer data is discussed further in Neilson et al. [2010].

Determination of TZTS Parameter Bounds

Latin Hypercube sampling was used to define the feasible parameter space for optimization and to understand relationships between model results at different locations within the study reach. The 15 parameters consisted of the seven calibration parameters identified previously (β, $A_{c,STS}$, α_{STS}, Y_{HTS}, Q_{HTS}, B_{tot}, n) for Section 1 and Section 2. The last parameter, depth of the ground conduction layer (Y_{gr}), is necessary for estimating heat transfer with the deeper sediments and is assumed to be the same for both Section 1 and Section 2.

The selection of an appropriate goodness-of-fit measure should be based on the characteristics of the data that are most important to capture. Similarly, the data used in the calculation of the goodness-of-fit measure should represent different system characteristics that are related through common parameters. From 6,000 sensitivity simulations, goodness-of-fit measures were tested to determine which provided the most information about the two-zone model based on the different data sets collected. We selected the Nash-Sutcliffe efficiency (*NSE*) which is defined as:

$$NSE = 1 - \frac{\sum_{i=1}^{N}(O_i - P_i)^2}{\sum_{i=1}^{N}(O_i - \overline{O})^2} \quad (8)$$

where O_i and P_i are the observed and predicted values for data set i and $\overline{O}$ is the mean observed value. The *NSE* ranges from minus infinity to 1, with values closer to 1 indicating that the predictions match the observations more closely [*Nash and Sutcliffe*, 1970]. A *NSE* value of 0 implies that the model gives no more information than a simple mean. This objective function was selected because high *NSE* values resulted in the best visual fit of most portions of the observations. For the calibrations, (1–*NSE*) was used instead of *NSE* because the objective function is minimized in these algorithms.

Objective function values calculated from observed and predicted temperature time series were the basis for setting the appropriate parameter bounds for optimization. The subset of observations selected arbitrarily for use in the sensitivity analysis included the MC temperatures at CS 2, MC temperatures at CS 3, and MC and STS solute concentrations at CS 3. *NSE* were calculated for each of these time series for 6000 simulations. *NSE* values greater than 0.9 for each individual observed time series and the corresponding parameter sets were defined as acceptable. All acceptable parameter sets were pooled to establish the parameter bounds for optimization.

TZTS Model Calibration Using SCEM and MOSCEM

MOSCEM uses the concept of Pareto dominance to determine the optimal parameter sets based on multiple objectives. Vrugt et al. [2003b] state that incompleteness or errors in model structure and errors in the data can prevent the occurrence of a parameter set where all objective functions have their minima. Therefore, a Pareto solution represents a parameter set that is impossible to distinguish as being objectively better than any other Pareto solution in the absence of more information [*Gupta et al.*, 1998]. Gupta et al. [1998] additionally point out that each of the Pareto solutions represent one characteristic of the data better than the others. An example of the resulting Pareto set of solutions is shown in Figure 5. The large dot represents a "fair" compromise between the two objective functions which is found by determining the Pareto solution with the smallest Euclidean distance from the origin. The parameter set associated with this solution is declared as the best representation of both objective functions. Moving along the Pareto solution between A and B results in a tradeoff between the objectives where an improvement in one objective function results in a deterioration of the other [*Vrugt et al.*, 2003b].

The calibrations within this study begin with single objective calibrations at two locations to investigate model results for the most common temperature model calibration approaches. These initial TZTS calibrations employ SCEM and use MC temperature observations in calibration at CS 2 and then CS 3. To consider the tradeoff associated with attempting to match multiple data sets in calibration, we then present the multiobjective calibration to temperatures in the MC at CS 2 and CS 3 simultaneously. To provide more information about how representative the calibrations are, the model results in each of the zones are presented and compared to the corresponding observations.

Results

Determination of TZTS Parameter Bounds

The results of the Latin Hypercube sampling used to establish parameter bounds are shown in Table 2. The parameters sets corresponding to *NSE* >0.9 for MC temperatures at CS 2 resulted in somewhat narrow bounds (shaded areas) for the MC temperatures at both CS 2 (Figure 6a) and CS 3 (Figure 6b). This figure suggests that the parameter estimates from a good fit at CS 2 will support a reasonable fit at CS 3. Similarly, model simulations using accepted parameter sets for observed MC temperatures at CS 3 indicate that the predictions for the MC at CS 3 (Figure 7b) do not include the data in portions of the diel cycle; however, the bounds on the predictions are narrow. Figure 7a shows that MC temperatures at CS 2 are well predicted using parameters based on observations at CS 3.

TZTS Model Calibration Using SCEM and MOSCEM

With the parameter bounds established by the Latin Hypercube sampling, the TZTS model was calibrated by minimizing (1–*NSE*) for MC temperatures using two different single objectives in SCEM (Figure 8 and 9) and the same two objectives simultaneously in MOSCEM (Figure 11). Each subplot (a-f) within these figures shows the model results and observations for

each zone (MC, STS, and HTS), and location (CS 2 and CS 3) being modeled. Observations (black) and model results (gray) are shown for data from the MC being used in calibration. Other time series are also displayed to corroborate whether the parameter sets from each calibration accurately represent the system as a whole. Both the river left (solid black line) and river right (dashed black line) STS observations are plotted for both CS 2 and 3. HTS observations are also shown in black with the solid line = 3 cm deep, dashed line = 9 cm deep, and dotted line = 20 cm deep. Note that at 0.5 days the sediment temperature probes were buried by moving sand at CS 3. At 1.3 days, these probes were uncovered, and were relocated where the sand was less likely to shift.

The single objective calibration results for MC temperatures at CS 2 reproduced temperatures in the MC (Figure 8a) and STS (Figure 8c) quite well at this cross-section. It is expected that given the simple representation of the hyporheic zone, the model predictions for this zone would reflect an average of the observations at 3, 9, and 20 cm depth. For this calibration, the HTS predictions at CS 2 (Figure 8e), however, underestimate the observations and have only a minor diel pattern.

The predictions at CS 3, using the optimal parameter set based on the CS 2 calibration, for the MC (Figure 8b) and STS (Figure 8d) represent some time periods well, but the bulk of the first day of the simulation does not match the observations. Both the maximum and minimum temperatures are over and underestimated, respectively. Similar to the HTS predictions at CS 2, the HTS predictions at CS 3 (Figure 8f) are consistently underestimated. The limited diel fluctuation within this zone suggests only minor influence from exchange with the surface water.

The single objective results for CS 3 reproduced the MC observations (Figure 9b) reasonably well, however, many of the observations were still not captured. Similar to the CS 2 single objective calibration, this calibration also over and under estimates the maximum and minimum temperatures, but the predictions are closer in magnitude to the observations. The STS results (Figure 9d) at CS 3 are similar to the MC, but the results between approximately 0.8-1.4 days closely matched the river left STS temperatures. Similar to the results from the previous single objective calibration, the HTS predictions (Figure 9f) at CS 3 are relatively flat and show little influence from the MC.

Using the parameter sets estimated from the MC temperatures at CS 3, the MC (Figure 9a) and STS temperature (Figure 9c) predictions at CS 2 are more representative for the first day. After that, they are less so due to the model underestimating temperatures until approximately 1.4 days. The associated HTS predictions (Figure 9e) at CS 2 have a larger diel amplitude and are closer to the 20 cm HTS observations.

The parameter sets for the last 300 simulations of the 3000 single objective optimization runs were normalized to between 0 and 1 by subtracting the estimated parameter values from their lower bounds and dividing by their range to create a relative scale (Figure 10). The subplots represent values for the MC temperature calibration at CS 2 for the upper (Figure 10a) and lower section (Figure 10b) and for the MC temperature calibration at CS 3 for both the upper (Figure 10c) and lower section (Figure 10d). A large amount of scatter suggests that the parameter was not repeatedly identified within these last iterations and the amount of information contained within the calibration data set was likely inadequate to identify this parameter.

For the multi-objective case, the objective functions (1−*NSE*) for MC temperatures at both CS 2 and CS 3 were minimized (Figure 11a and 11b, respectively). The predicted temperatures for the MC at CS 2 matches the observations well; however, the temperatures are underestimated at CS 3 after approximately 0.3 days. Figure 11c and 11d show the results for the STS at CS 2 and 3, respectively. Figure 11c shows that the STS temperatures are very similar to the two sets of observations. STS temperatures at CS 3 (Figure 11d) match the peak of the river right observations the first day, and then follow the river left the following day. The minimum temperatures, similar to the MC, are underestimated. Figure 11e and 11f show that the HTS model predictions are within the bounds of the three depths of hyporheic temperature observations and display a greater diel fluctuation that more closely represents an average of the three sediment temperature data sets. The hyporheic temperatures at CS 3 (Figure 11f), however, lie within the bounds of the three depths of observations for the first 0.5 days until the temperature probes were buried by moving sand.

Although the "best" compromise solution was chosen as the set with the shortest Euclidian distance to the origin as in Figure 5, it is important to highlight that all the parameter sets along the Pareto front are indistinguishable from each other in terms of their ability to minimize both objective functions. We found that the bounds corresponding to all the parameter sets associated with the Pareto front for the MC temperatures at CS 2 and CS 3 resulted in very narrow temperature bounds. Plots of these results are nearly identical to Figure 11 and therefore, are not included here. Table 3 presents the optimal parameter sets for each of the three optimization runs.

Discussion

The TZTS model provides a simplified representation of both the sediments below the MC flow (HTS) and stagnant areas near the edges of the channel (STS) and assumes first-order exchange with each of these zones. While simple, the resulting number of parameters requiring estimation significantly increased from a basic instream temperature model that only accounts for surface fluxes. This made manual calibration of the model difficult and led to the use of an automatic optimization algorithm. The resulting calibrations were corroborated using observed temperature data for the same time period at locations along the study reach and at various zones within each cross-section.

As the Latin Hypercube and SCEM results demonstrate (Figure 6 -9), the single objective calibrations show that the best parameter set for the MC temperatures at CS 2 produces a reasonable, but not necessarily good, fit of the MC temperatures at CS 3. The last 300 parameter sets associated with each calibration illustrates that when using information at CS 2 for calibration, the ability to confidently identify parameter sets at CS 3 is difficult as shown by the large amount of scatter in all of the parameters for the lower section (Figure 10b). When information is used at CS 3, however, the ability to identify the parameters in both sections is notably better (Figure 10c and d) which supports the conclusion that the temperatures at these two locations are related.

The STS and HTS observations, being used only as corroboration data, provide insight into the ability of the model to represent dominant processes that control temperature responses in each of these storage zones at the reach scale when using only one set of MC temperatures for

calibration. The STS temperature predictions for each single objective calibration (Figures 8 and 9) illustrate that if the MC temperatures are predicted well, that the STS temperature predictions can be expected to also be reasonable. This is consistent with results from tracer studies in these reaches that consistently showed fast exchange between these zones (see *Neilson et al.* [2010]). HTS temperature predictions were typically poor when using information only from the MC at one location, implying that the calibration data set did not contain enough pertinent information to estimate the parameters associated with this zone. Interestingly, the last 300 parameter sets associated with the single objective calibration show that the parameters associated with the HTS (Q_{HS} and Y_{HS}) have little scatter and indicate some level of confidence (Figure 10a,c,d). However, Y_{gr} (depth of ground), which has a large impact on the HTS predictions, consistently shows a large amount of scatter. These results suggest that the MC temperatures provide little information regarding Y_{gr} since it only indirectly affects the MC via the HTS zone. This highlights the importance of collecting information to provide a boundary condition within the deeper sediments (e.g., >1 m deep temperature measurements in the bed substrate to serve as a lower boundary condition). This type of supporting data would also decrease the parameter space being sampled and would result in more confidence in the remaining parameter estimates.

While the single objective calibrations do not appear to capture the mechanisms necessary to accurately predict temperatures within the HTS, when data are provided in the MC at both CS 2 and CS 3, the associated tradeoff appears to highlight the dominant processes and provide more information about the corresponding parameters. The two-objective calibration not only captured the MC temperatures at each location, it additionally reproduced the temperatures in each zone at each location reasonably well (Figure 11). Even though these results are

significant, nearly every parameter in the optimal parameter set from the two-objective results was near the bounds established from the Latin Hypercube sampling. This could mean that a different method for establishing the parameter bounds may be necessary (e.g., consider the *NSE* for other zones than the MC). The model prediction bounds associated with the tradeoff between the two objectives resulted in predictions that were almost identical to those based on the optimal parameter set. This suggests the uncertainty from these estimated parameters is relatively small when predicting instream temperatures. The results of the two-objective optimization further highlight the utility of using multiple lines of evidence in multi-zone temperature model calibration, especially when compared to the single-objective optimizations.

Another interesting result of the optimizations is the differences in the optimal parameter sets for each of the calibrations (Table 3). For the single objective calibration, the B_{tot}, n, β, $A_{c\ STS}$ for the upper section are consistently estimated. The differences primarily lie in the α_{STS}, Q_{HTS}, and Y_{HTS}. As would be expected due to the lack of information in this portion of the study reach, the parameter estimates for the lower section are much more variable. The parameters associated with the two-objective calibration are different than each single-objective calibration. Additional supporting data types, such as tracer studies, could provide more information regarding various instream processes and may assist in more confidently identifying parameters (see *Neilson et al.* [2010]). It is also possible to decrease the number of parameters requiring estimation using other data such as spatially distributed multispectral and thermal imagery to estimate B_{tot} and β [*Bingham et al.* 2010]. Having fewer estimated parameters tends to decrease parameter uncertainty and improve overall temperature modeling results within each zone.

In a companion paper (Neilson et al. [2009]), we compute the relative magnitude of the STS and HTS fluxes associated with the two-objective temperature calibration from the current paper. We found that the HTS is a heat sink at night and in early morning, and a heat source in the mid-morning through the evening which creates a lagged and buffered MC temperature response. This is consistent with other studies that have found that exchange with the HTS zone induces a lag in instream temperatures and results in smaller diel fluctuations [*Johnson*, 2004; *Loheide and Gorelick*, 2006]. Similar to what we observed in the sediment temperatures in the Virgin River, many have found that the combined effect of bed conduction and advective exchange with the hyporeheic zone creates lagged and buffered temperatures within the sediments [*Arrigoni et al.*, 2008; *Evans and Petts*, 1997; *Silliman and Booth*, 1993; *Silliman et al.*, 1995].

With respect to STS, Rutherford [1993] found near bank temperatures to be lower than the main channel average (0.03-0.05 C) and suggested that some sites may need to represent shallow areas differently due to faster heating and cooling of these areas. Clark [1999] found warmer temperatures in dead zones by 3 °C during the day and 4.5 °C lower in the night. For this Virgin River case study, we (Neilson et al. [2009]) found both warmer and cooler temperatures in near shore STS during the day depending on the location, depth, and shading. Further, our model results in this paper indicate that the STS zone is a heat source at night and a heat sink during a portion of the day, however, the relative magnitude of this heat flux was less significant that the HTS

Conclusions

The TZTS model was formulated to represent streams and rivers as a system of completely mixed, but interconnected zones that can capture the dominant mechanisms associated with heat and solute dynamics at the reach scale. These processes include advection through the MC, surface fluxes with the MC and STS, advective exchange with both the STS and HTS, and conduction with the HTS and deeper ground. By including temperature within the model, it was necessary to develop a more detailed parameterization than is typically used for transient storage modeling of simple tracers. The large number of parameters requiring estimation was addressed through single and multiple objective optimization algorithms. Observed temperature data collected within each of these zones at several locations within the study reach were used for model calibration and corroboration.

In general, we found that *in-situ* temperature observations from each storage zone provide much of the necessary information necessary to determine the effectiveness of the model and calibration approach. These observations illustrated the limitations of single objective calibration to capture the processes occurring within STS and HTS zones for this case study. In calibrating to MC temperatures, the accuracy of model predictions at two different locations along the study reach was dependent on the relative spatial location of the observations used in calibration. For each calibration, if MC temperatures were well predicted, the associated STS temperatures were also well predicted. The HTS results, however, were consistently poor. The results of the two-objective calibration that simultaneously used MC temperatures from two locations along the study reach resulted in accurate predictions within each of the two zones at both locations in the study reach. These results suggest that effective parameter estimation for

multi-zone stream models requires multiple data series to capture the temperature responses within each zone.

Acknowledgements

We would like to acknowledge the Graduate Assistance for Areas of National Need (GAANN) fellowship that funded this research. We are indebted to our field crews (Quin Bingham, Andrew Neilson, Amber Spackman, Kiran Chinnayakanahalli, Tenielle Beckstead, Jeremy Butterbaugh). We would also like to thank Steve Meismer at the Washington County Water Conservancy District, Rick Fridell and Amos Rehm at the Utah Division of Wildlife Resources for their support of this research, Drs. Yasir Kaheil and Enrique Rosero for their assistance and insight, and Dr. Anders Wörman for his thoughtful comments regarding the manuscript.

Appendix 1: Derivation of TZTS model equations

Discrete forms of the heat balance equations can be written for the *i*th control volume of the main channel assuming constant channel geometry. Heat and mass transfer between the main channel and each storage zone is based on Fick's law.

Main Channel Heat Balance Equations

$$\rho C_p V_{MC} \frac{dT_{MC,i}}{dt} = Q_{MC,i-1}\rho C_p T_{MC,i-1} - Q_{MC,i}\rho C_p T_{MC,i} + \frac{D}{\Delta x_i} B_{MC,i} Y_{MC,i} \rho C_p (T_{MC,i-1} - T_{MC,i}) + \frac{D}{\Delta x_i} B_{MC,i} Y_{MC,i} \rho C_p (T_{MC,i+1} - T_{MC,i}) +$$

$$J_{atm} B_{MC,i} \Delta x_i + \rho C_p \alpha_{STS,i} \frac{Y_{STS,i} \Delta x_i}{B_{STS,i}} (T_{STS,i} - T_{MC,i}) + \rho C_p \alpha_{HTS,i} \frac{\Delta x_i B_{HTS,i}}{Y_{HTS,i}} (T_{HTS,i} - T_{MC,i}) +$$

$$\rho_{sed,i} C_{p,sed,i} \alpha_{sed,i} \left(\frac{T_{HTS,i} - T_{MC,i}}{Y_{HTS}} \right) B_{MC} \Delta x_i \qquad \text{(A1)}$$

Figure A1 shows a cross sectional schematic of the model structure and the associated parameters. The terms describing the longitudinal transport are shown in Figure 1.

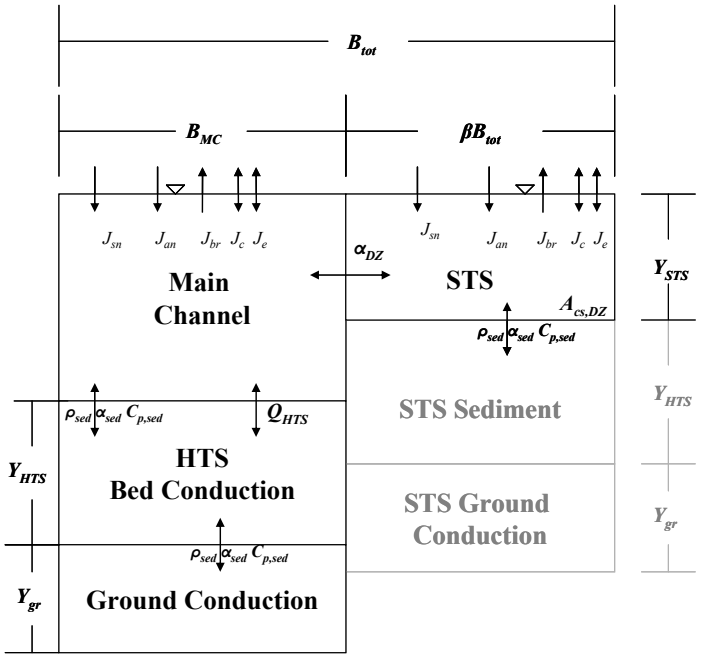

Figure A1. Model structure.

The volume of a main channel reach is defined as

$$V_{MC} = B_{MC} Y_{MC} \Delta x \tag{A2}$$

Dividing Eqn. 1 by ρ, C_p, and V_{MC} (Eqn. 2):

$$\frac{dT_{MC,i}}{dt}=\frac{Q_{MC,i-1}\rho C_p T_{MC,i-1}}{\rho C_p B_{MC,i} Y_{MC,i}\Delta x_i}-\frac{Q_{MC,i}\rho C_p T_{MC,i}}{\rho C_p B_{MC,i} Y_{MC,i}\Delta x_i}+\frac{D}{\Delta x_i}\frac{B_{MC,i} Y_{MC,i}\rho C_p (T_{MC,i-1}-T_{MC,i})}{\rho C_p B_{MC,i} Y_{MC,i}\Delta x_i}+\frac{D}{\Delta x_i}\frac{B_{MC,i} Y_{MC,i}\rho C_p (T_{MC,i+1}-T_{MC,i})}{\rho C_p B_{MC,i} Y_{MC,i}\Delta x_i}+$$

$$\frac{J_{atm} B_{MC,i}\Delta x_i}{\rho C_p B_{MC,i} Y_{MC,i}\Delta x_i}+\frac{\rho C_p \alpha_{STS,i}\frac{Y_{STS,i}\Delta x_i}{B_{STS,i}}(T_{STS,i}-T_{STS,i})}{\rho C_p B_{MC,i} Y_{MC,i}\Delta x_i}+\frac{\rho C_p \alpha_{HTS,i}\frac{\Delta x_i B_{HTS,i}}{Y_{HTS,i}}(T_{HTS,i}-T_{MC,i})}{\rho C_p B_{MC,i} Y_{MC,i}\Delta x_i}+$$

$$\frac{\rho_{sed,i} C_{p,sed,i}\alpha_{sed,i}\left(\frac{T_{HTS,i}-T_{MC,i}}{Y_{HTS}}\right)B_{MC}\Delta x_i}{\rho C_p B_{MC,i} Y_{MC,i}\Delta x_i} \qquad \text{(A3)}$$

Canceling terms:

$$\frac{dT_{MC,i}}{dt}=\frac{Q_{MC,i-1}T_{MC,i-1}}{B_{MC,i} Y_{MC,i}\Delta x_i}-\frac{Q_{MC,i}T_{MC,i}}{B_{MC,i} Y_{MC,i}\Delta x_i}+D\frac{(T_{MC,i-1}-T_{MC,i})}{\Delta x_i^2}+D\frac{(T_{MC,i+1}-T_{MC,i})}{\Delta x_i^2}+$$

$$\frac{J_{atm}}{\rho C_p Y_{MC,i}}+\frac{\alpha_{STS,i} Y_{STS,i}(T_{STS,i}-T_{MC,i})}{B_{STS,i} B_{MC,i} Y_{MC,i}}+\frac{\alpha_{HTS,i} B_{HTS,i}(T_{HTS,i}-T_{MC,i})}{B_{MC,i} Y_{MC,i} Y_{HTS,i}}+ \qquad \text{(A4)}$$

$$\frac{\rho_{sed,i} C_{p,sed,i}\alpha_{sed,i}(T_{HTS,i}-T_{MC,i})}{\rho C_p Y_{MC,i} Y_{HTS}}$$

Q_{HTS} is defined as:

$$Q_{HTS,i}=\alpha_{HTS,i}\frac{B_{HTS,i}\Delta x}{Y_{HTS,i}} \qquad \text{(A5)}$$

Substituting Q_{HTS} into Eqn. 4:

$$\frac{dT_{MC,i}}{dt} = \frac{Q_{MC,i-1}T_{MC,i-1}}{B_{MC,i}Y_{MC,i}\Delta x_i} - \frac{Q_{MC,i}T_{MC,i}}{B_{MC,i}Y_{MC,i}\Delta x_i} + D\frac{(T_{MC,i-1}-T_{MC,i})}{\Delta x_i^2} + D\frac{(T_{MC,i+1}-T_{MC,i})}{\Delta x_i^2} + \frac{J_{atm}}{\rho C_p Y_{MC,i}} + \frac{\alpha_{STS,i}Y_{STS,i}(T_{STS,i}-T_{MC,i})}{B_{STS,i}B_{MC,i}Y_{MC,i}} + \frac{Q_{HTS,i}(T_{HTS,i}-T_{MC,i})}{B_{MC,i}Y_{MC,i}\Delta x_i} + \frac{\rho_{sed,i}C_{p,sed,i}\alpha_{sed,i}(T_{HTS,i}-T_{MC,i})}{\rho C_p Y_{MC,i}Y_{HTS}} \quad \text{(A6)}$$

Defining $B_{STS} = \beta_i B_{tot,i}$, multiplying the dead-zone term by $\frac{B_{STS}}{B_{STS}}$:

$$\frac{dT_{MC,i}}{dt} = \frac{Q_{MC,i-1}T_{MC,i-1}}{B_{MC,i}Y_{MC,i}\Delta x_i} - \frac{Q_{MC,i}T_{MC,i}}{B_{MC,i}Y_{MC,i}\Delta x_i} + D\frac{(T_{MC,i-1}-T_{MC,i})}{\Delta x_i^2} + D\frac{(T_{MC,i+1}-T_{MC,i})}{\Delta x_i^2} + \frac{J_{atm}}{\rho C_p Y_{MC,i}} + \frac{\alpha_{STS,i}Y_{STS,i}B_{STS,i}(T_{STS,i}-T_{MC,i})}{(\beta B_{TOT})^2 B_{MC,i}Y_{MC,i}} + \frac{Q_{HTS,i}(T_{HTS,i}-T_{MC,i})}{B_{MC,i}Y_{MC,i}\Delta x_i} + \frac{\rho_{sed,i}C_{p,sed,i}\alpha_{sed,i}(T_{HTS,i}-T_{MC,i})}{\rho C_p Y_{MC,i}Y_{HTS}} \quad \text{(A7)}$$

Combining terms, results in:

$$\frac{dT_{MC,i}}{dt} = \frac{Q_{MC,i-1}T_{MC,i-1}}{V_{MC,i}} - \frac{Q_{MC,i}T_{MC,i}}{V_{MC,i}} + D\frac{(T_{MC,i-1} - T_{MC,i})}{\Delta x_i^2} + D\frac{(T_{MC,i+1} - T_{MC,i})}{\Delta x_i^2} +$$

(Advection) (Dispersion)

$$\frac{J_{atm}}{\rho C_p Y_{MC,i}} + \frac{\alpha_{STS,i} A_{cs,STS,i}}{A_{cs,MC,i}(\beta B_{tot})^2}(T_{STS,i} - T_{STS,i}) + \frac{Q_{HTS,i}}{V_{MC,i}}(T_{HTS,i} - T_{MC,i}) +$$

(Surface Fluxes) (J_{STS}) (J_{HTS})

$$\frac{\rho_{sed,i} C_{p,sed,i} \alpha_{sed,i}}{\rho C_p Y_{MC,i} Y_{HTS,i}}(T_{HTS,i} - T_{MC,i})$$

(J_{bed})

(A8)

where T = temperature (°C), Q = volumetric flow rate (m^3s^{-1}), V = volume of zone (m^3), D = longitudinal dispersion (m^2d^{-1}), Δx = volume length (m), $\alpha_{STS,i}$ = exchange between the MC and the STS (m^2d^{-1}), $Q_{HTS,i}$ = HTS advective transport coefficient (m^3d^{-1}), A_{cs} = cross-sectional area of zone (m^2), B_{tot} = total volume width (m), β = the STS fraction of the total channel width, Y = volume depth (m), ρ = density of the water (g cm^{-3}), C_p = heat capacity of the water (cal $g^{-1}{}^{o}C^{-1}$), ρ_{sed} = density of the sediment (g cm^{-3}), $C_{p,sed}$ = heat capacity of the sediment (cal $g^{-1}{}^{o}C^{-1}$), α_{sed}= coefficient of thermal diffusivity of the sediment, and J_{atm} = air-water interface fluxes (cal $cm^{-2}s^{-1}$) as defined in Eqn. 2. The subscripts $i - 1$ and $i + 1$ designate the contiguous upstream and downstream volumes, respectively, and the subscripts *MC*, *STS*, *HTS,* and *gr* specify the main channel, surface transient storage, hyporheic transient storage, and ground layer, respectively.

1 Notice that the advection, dispersion, surface storage, and hyporheic storage terms in this

2 equation are identical to those used to model solute transport in Neilson et al. [2010].

Dead-Zone Heat Balance Equations

$$\rho C_p V_{STS} \frac{dT_{STS,i}}{dt} = J_{atm,STS}\beta_i B_{tot,i}\Delta x_i + \rho C_p \alpha_{STS,i} \frac{Y_{STS,i}\Delta x_i}{\beta_i B_{tot,i}}(T_{MC,i} - T_{STS,i}) + \rho_{sed,i} C_{p,sed,i} \alpha_{sed,i} \left(\frac{T_{STS,sed,i} - T_{STS,i}}{Y_{HTS}} \right) \beta_i B_{tot,i} \Delta x_i \quad \text{(A9)}$$

Dividing by ρ, C_p, and $V_{STS} = \beta_i B_{tot,i} Y_{STS} \Delta x$:

$$\frac{dT_{STS,i}}{dt} = \frac{J_{atm,STS}\beta B_{tot,i}\Delta x_i}{\rho C_p V_{STS}} + \frac{\rho C_p \alpha_{STS,i} \frac{Y_{STS,i}\Delta x_i}{\beta B_{tot,i}}(T_{MC,i} - T_{STS,i})}{\rho C_p V_{STS}} + \frac{\rho_{sed,i} C_{p,sed,i} \alpha_{sed,i} \left(\frac{T_{STS,sed,i} - T_{STS,i}}{Y_{HTS}} \right) \beta B_{tot,i} \Delta x_i}{\rho C_p V_{STS}} \quad \text{(A10)}$$

Canceling terms:

$$\boxed{\frac{dT_{STS,i}}{dt} = \frac{J_{atm,STS}}{\rho C_p Y_{STS}} + \frac{\alpha_{STS,i}}{(\beta B_{tot,i})^2}(T_{MC,i} - T_{STS,i}) + \frac{\rho_{sed,i} C_{p,sed,i} \alpha_{sed,i}}{\rho C_p Y_{STS} Y_{HTS}}(T_{STS,sed,i} - T_{STS,i})} \quad \text{(A11)}$$

Dead-Zone Sediment Heat Balance Equations

$$\rho C_p V_{STS,sed} \frac{dT_{STS,sed,i}}{dt} = \rho_{sed,i} C_{p,sed,i} \alpha_{sed,i} \left(\frac{T_{STS,i} - T_{STS,sed,i}}{Y_{HTS}} \right) \beta_i B_{tot,i} \Delta x_i + \rho_{sed,i} C_{p,sed,i} \alpha_{sed,i} \left(\frac{T_{gr,i} - T_{STS,sed,i}}{Y_{gr}} \right) \beta_i B_{tot,i} \Delta x_i \quad \text{(A12)}$$

Dividing by ρ, C_p, and $V_{STS,sed} = \beta_i B_{tot,i} Y_{HTS} \Delta x$:

$$\frac{dT_{STS,sed,i}}{dt} = \frac{\rho_{sed,i} C_{p,sed,i} \alpha_{sed,i} \left(\frac{T_{STS,i} - T_{STS,sed,i}}{Y_{HTS}} \right) \beta_i B_{tot,i} \Delta x_i}{\rho C_p V_{STS,sed}} + \frac{\rho_{sed,i} C_{p,sed,i} \alpha_{sed,i} \left(\frac{T_{gr,i} - T_{STS,sed,i}}{Y_{gr}} \right) \beta_i B_{tot,i} \Delta x_i}{\rho C_p V_{STS,sed}} \quad \text{(A13)}$$

This assumes that the depth over which conduction is occurring below the dead zone is equal to that of the main channel (i.e., Y_{HTS}). Canceling out terms:

$$\boxed{\frac{dT_{STS,sed,i}}{dt} = \frac{\rho_{sed,i} C_{p,sed,i} \alpha_{sed,i}}{\rho C_p Y_{HTS}^2} (T_{STS,i} - T_{STS,sed,i}) + \frac{\rho_{sed,i} C_{p,sed,i} \alpha_{sed,i}}{\rho C_p Y_{HTS} Y_{gr}} (T_{gr,i} - T_{STS,sed,i})} \quad \text{(A14)}$$

Hyporheic Storage Heat Balance Equations

$$\rho C_p V_{HTS} \frac{dT_{HTS,i}}{dt} = \rho C_p \alpha_{HTS,i} \frac{\Delta x_i B_{HTS,i}}{Y_{HTS,i}} (T_{MC,i} - T_{HTS,i}) + \rho_{sed,i} C_{p,sed,i} \alpha_{sed,i} \left(\frac{T_{MC,i} - T_{HTS,i}}{Y_{HTS}} \right) B_{MC} \Delta x_i + \rho_{sed,i} C_{p,sed,i} \alpha_{sed,i} \left(\frac{T_{gr,i} - T_{HTS,i}}{Y_{gr}} \right) B_{MC} \Delta x_i \quad \text{(A15)}$$

Dividing by ρ, C_p, and $V_{HTS} = B_{HTS} Y_{HTS} \Delta x$:

$$\frac{dT_{HTS,i}}{dt} = \frac{\rho C_p \alpha_{HTS,i} \frac{\Delta x_i B_{HTS,i}}{Y_{HTS,i}} (T_{MC,i} - T_{HTS,i})}{\rho C_p V_{HTS}} + \frac{\rho_{sed,i} C_{p,sed,i} \alpha_{sed,i} \left(\frac{T_{MC,i} - T_{HTS,i}}{Y_{HTS}} \right) B_{MC} \Delta x_i}{\rho C_p V_{HTS}} + \frac{\rho_{sed,i} C_{p,sed,i} \alpha_{sed,i} \left(\frac{T_{gr,i} - T_{HTS,i}}{Y_{gr}} \right) B_{MC} \Delta x_i}{\rho C_p V_{HTS}} \quad \text{(A16)}$$

Setting $B_{HTS} = B_{MC}$, canceling terms and substituting in Q_{HTS}:

$$\boxed{\frac{dT_{HTS,i}}{dt} = \frac{Q_{HTS}}{V_{HTS}} (T_{MC,i} - T_{HTS,i}) + \frac{\rho_{sed,i} C_{p,sed,i} \alpha_{sed,i}}{\rho C_p Y_{HTS}^2} (T_{MC,i} - T_{HTS,i}) + \frac{\rho_{sed,i} C_{p,sed,i} \alpha_{sed,i}}{\rho C_p Y_{HTS} Y_{gr}} (T_{gr,i} - T_{HTS,i})} \quad \text{(A17)}$$

Appendix 2: Numerical solution method

Using upwind spatial differencing and setting longitudinal dispersion to zero, Eq. (8) becomes,

$$\frac{dC_{MC,i}}{dt} = \frac{Q_{MC,i-1}C_{MC,i-1}}{V_{MC,i}} - \frac{Q_{MC,i}C_{MC,i}}{V_{MC,i}} + \frac{\alpha_{STS,i}A_{cs,STS,i}}{A_{cs,MC,i}(\beta_i B_{tot,i})^2}(C_{STS,i} - C_{MC,i}) + \frac{Q_{HTS,i}}{V_{MC,i}}(C_{HTS,i} - C_{MC,i}) \quad \text{(A18)}$$

where $C_{MC,i}^{t+\Delta t}$ = main-channel concentration at $t + \Delta t$. This equation can be solved for

$$C_{MC,i}^{t+\Delta t} = \left[\frac{Q_{MC,i-1}C_{MC,i-1}}{V_{MC,i}} - \frac{Q_{MC,i}C_{MC,i}}{V_{MC,i}} + \frac{\alpha_{STS,i}A_{cs,STS,i}}{A_{cs,MC,i}(\beta_i B_{tot,i})^2}(C_{STS,i} - C_{MC,i}) + \frac{Q_{HTS,i}}{V_{MC,i}}(C_{HTS,i} - C_{MC,i})\right]\Delta t \quad \text{(A19)}$$

This equation was solved numerically using Euler's method.

A Taylor series analysis was used to determine that such a forward-time, backward space solution scheme has numerical dispersion which can be estimated with [*Chapra*, 1997]

$$D_n = 0.5U\Delta x - 0.5U^2\Delta t \quad \text{(A19)}$$

where D_n = numerical dispersion (m^2/d), and Δt = the integration time step (d).

If the actual physical dispersion, D, is known, and Δx is specified, we can set $D_n = D$ and solve Eqn. (18) for

$$\Delta t = \frac{U\Delta x - 2D}{U^2} \tag{A20}$$

Using this time step will yield a numerical dispersion equivalent to the physical dispersion.

References

Arrigoni, A. S., G. Poole, L. A. K. Mertes, S. J. O'Daniel, W. Woessner, and S. A. Thomas (2008), Buffered, lagged, or cooled? Disentangling hyporheic influences on temperature cycles in stream channels., *Water Resources Research*, *44*(W09418), 13.

Bencala, K. E., and R. A. Walters (1983), Simulation of solute transport in a mountain pool-and-riffle stream: a transient storage model, *Water Resources Research*, *19*(3), 718-724.

Beschta, R. L., and J. Weatherred (1984), TEMP-84 A computer model for predicting stream temperatures resulting fromt he management of streamside vegetation., edited by W. S. D. G. Forest Service, United States Department of Agriculture.

Beschta, R. L., and J. Weatherred (1987), TEMP-86 Users Guide Department of Engineering*Rep.*, Oregon State University, Corvallis, OR.

Bingham, Q. B., B.T. Neilson, C.M.U. Neale, M.B. Cardenas (2010), Delineation of dead zones in rivers using remotely sensed data and their utility in improving two-zone temperature and solute transport model performance. Journal of Hydrology. In review.

Boyd, M., and B. Kasper (2003), Analytical methods for dynamic open channel heat and mass transfer, methodology for the Heat Source Model version 7.0*Rep.*, Carollo Engineers.

Briggs, M. A., M. N. Gooseff, C. D. Arp, and M. A. Baker (2009), A Method for Estimating Surface Transient Storage Parameters for Streams with Concurrent Hyporheic Exchange, *Water Resources Research*, *45(*W00D27).

Chapra, S. (2006), Sediment-water heat exchange in surface water quality models, Medford, MA.

Chapra, S. C. (1997), *Surface Water Quality Modeling*, McGraw-Hill, Boston, MA.

Chapra, S. C., G. J. Pelletier, and H. Tao (2004), QUAL2K: A Modeling Framework for Simulating River and Stream Water Quality, Version 1.3: Documentation and Users Manual., edited, Civil and Environmental Engineering Dept., Tufts University, Medford, MA.

Choi, J., J. W. Harvey, and M. H. Conklin (2000), Characterizing multiple timescales of stream and storage zone interaction that affect solute fate and transport in streams, *Water Resources Research*, *36*(6), 1511-1518.

Clark, E., B. W. Webb, and M. Ladle (1999), Microthermal gradients and ecological implications in Dorset Rivers, *Hydrological Processes*, *13*, 423-438.

Constantz, J. (2008), Heat as a tracer to determine streambed water exchanges, *Water Resources Research*, *44*(W00D10).

Duan, Q., S. Sorooshian, and V. Gupta (1992), Effective and efficient global optimization for conceptual rainfall-runoff models, *Water Resources Research*, *28*(4), 1015-1031.

Evans, E. C., and G. E. Petts (1997), Hyporheic temperature patterns within riffles., *Hydrological Sciences*, *42*(2).

Gupta, H. V., S. Sorooshian, and P. O. Yapo (1998), Toward Improved Calibration of Hydrologic Models: Multiple and Noncommensurable Measures of Information, *Water Resources Research*, *34*(4), 751-763.

Harvey, J. W., and B. J. Wagner (2000), Streams and Ground Waters, in *Aquatic Ecology Series*, edited by J. B. Jones and P. J. Mulholland, p. 425, Academic Press, San Diego.

Harvey, J. W., B. J. Wagner, and K. E. Bencala (1996), Evaluating the reliability of the stream tracer approach to characterize stream-subsurface water exchange, *Water Resources Research*, *32*(8), 2441-2451.

Harvey, J. W., J. E. Saiers, and J. T. Newlin (2005), Solute transport and storage mechanisms in wetlands of the Everglades, south Florida, *Water Resources Research*, *41*(W05009), 1-14.

Hauser, G. E., and G. A. Schohl (2003), River Modeling System v.4 - User Guide and Technical Reference, edited, TVA River System Operations and Environment. Norris, Tennessee.

Herbert, L. R. (1995), Seepage Study of the Virgin River from Ash Creek to Harrisburg Dome, Washington County, Utah*Rep. Technical Publication no. 106*, 8 pp, United States Geological Survey/State of Utah Department of Natural Resources.

Hoffman, J. D. (2001), *Numerical Methods for Engineers and Scientists* Second Edition ed., 823 pp., Marcel Dekker, Inc., New York.

Johnson, S. L. (2004), Factors influencing stream temperature in small streams: substrate effects and a shading experiment, *Can. J. Fish. Aquat. Sci.*, *61*, 913-923.

Kazezyilmaz-Alhan, C. M., and M. A. Medina Jr. (2006), Stream solute transport incorporating hyporheic zone processes, *Journal of Hydrology*, *329*, 26-38.

Legates, D. R., and G. J. McCabe, Jr. (1999), Evaluating the use of goodness-of-fit measures in hydrologic and hydroclimatic model validation, *Water Resources Research*, *35*(1), 233-241.

Loheide, S. P., and S. M. Gorelick (2006), Quantifying stream-aquifer interactions through the analysis of remotely sensed thermographic profiles in in situ temperature histories, *Environmental Science and Technology*, *40*(10), 3336-3341.

Martin, J. L., and S. C. McCutcheon (1999), Data Requirements, in *Hydrodynamics and transport for water quality modeling*, edited, p. 794, Lewis Publishers, Boca Raton.

McCullough, D., S. Spalding, D. Sturdevant, and M. Hicks (2001), Issue Paper 5: Summary of Technical Literature Examining the Physiological Effects of Temperature on Salmonids, edited, EPA Region 10 Seattle, WA.

Nash, J. E., and J. V. Sutcliffe (1970), River flow forecasting through conceptual models part I: A discussion of principles, *Journal of Hydrology*, *10* (3), 282–290.

Neilson, B. T. (2006), Dynamic Stream Temperature Modeling: Understanding the Causes and Effects of Temperature Impairments and Uncertainty in Predictions, Dissertation thesis, Utah State University, Logan, UT.

Neilson, B. T., D. K. Stevens, S. C. Chapra, and C. Bandaragoda (2009), Data Collection Methodology for Dynamic Temperature Model Testing and Corroboration, *Hydrological Processes*, *23*, 2902-2914.

Neilson, B. T., S. C. Chapra, D. K. Stevens, and C. Bandaragoda (2010), Two zone transient storage modeling using temperature and solute data with multiobjective calibration: Part 2 temperature and solute, *Water Resources Research*, *In Review.*

Packman, A. I., and K. E. Bencala (2000), Streams and Ground Waters, in *Aquatic Ecology Series*, edited by J. B. Jones and P. J. Mulholland, p. 425, Academic Press, San Diego.

Runkel, R. L. (1998), One dimensional transport with inflow and storage (OTIS): A solute transport model for streams and rivers*Rep. 98-4018*, 73 pp, U.S. Geological Survey.

Runkel, R. L., and D. M. McKnight (2003), Preface: Modeling hyporheic zone processes, *Advances in Water Resources*, *26*, 901-905.

Rutherford, J. C., J. B. Macaskill, and B. L. Williams (1993), Natural water temperature variations inthe lowe Waikato River, New Zealand, *New Zealand Journal of Marine and Freshwater Research*, *27*, 71-85.

Sauter, S. T., J. McMillan, and J. Dunham (2001), Issue Paper 1: Salmonid Behavior and Water Temperature, edited, EPA Region 10. Seattle, WA, Washington, D.C.

Schoups, G., C. L. Addams, and S. M. Gorelick (2005a), Multi-Objective Calibration of a Surface Water-Groundwaterflow Model in an Irrigated Agricultural Region: Yaqui Balley, Sonora, Mexico, *Hydrology and Earth System Sciences*, *9*, 549-568.

Schoups, G., J. W. Hopmans, C. A. Young, J. A. Vrugt, and W. W. Wallender (2005b), Multi-Criteria Optimization of a Regional Spatially-Distributed Subsurface Water Flow Model, *Journal of Hydrology*, *311*, 20-48.

Silliman, S. E., and D. F. Booth (1993), Analysis of time-series measurements of sediment temperature for identification of gaining vs. losing portions of Juday Creek, Indiana, *Journal of Hydrology*, *146*, 131-148.

Silliman, S. E., J. Ramirez, and R. L. McCabe (1995), Quantifying downflow through creek sediments using temperature time series: one-dimensional solution incorporating measured surface temperature., *Journal of Hydrology*, *167*, 99-119.

Theurer, F. D., K. A. Voos, and W. J. Miller (1984), Instream water temperature model., edited, U.S. Fish and Wildlife Service.

Vrugt, J. A., H. V. Gupta, W. Bouten, and S. Sorooshian (2003a), A shuffled complex evolution metropolis algorithm for optimization and uncertainty assessment of hydrologic model parameters., *Water Resources Research*, *39*(8), 1201.

Vrugt, J. A., H. V. Gupta, L. A. Bastidas, W. Bouten, and S. Sorooshian (2003b), Effective and efficient algorithm for multiobjective optimization of hydrologic models, *Water Resources Research*, *39*(8), 1214.

Zaramella, M., and A. I. Packman (2003), Application of the transient storage model to analyze advective hyporheic exchange with deep and shallow sediment beds, *Water Resources Research*, *39*(7), 1198.

Table and Figure Captions

Table 1. Time series data collected and the related parameters.

Table 2. Parameter ranges determined from the Latin Hypercube sampling.

Table 3. Resulting best parameter sets for all three optimizations.

Figure 1. Two-zone model schematic of the connectivity between the main channel (MC), surface transient storage (STS), and subsurface or hyporheic transient storage (HTS).

Figure 2. Energy balance components of the two-zone temperature and solute model.

Figure 3. Virgin River study location (taken from Neilson et al. [2009]).

Figure 4. Locations of temperature probes at each of the three locations within the study reach (taken from Neilson et al. [2009]).

Figure 5. Example objective space emphasizing the Pareto solution set for a two-objective optimization. The larger black dot represents the optimal parameter set given both objectives as the criteria while the other slightly smaller dots represent the rest of the Pareto solution set. The small plus signs represent those that are not part of the Pareto solution set. The points labeled (A) and (B) represent the parameter sets resulting in the minimum value for each objective function.

Figure 6. Latin Hypercube sampling simulation results for: (a) MC temperatures at CS 2, (b) MC temperatures at CS 3 from parameter sets corresponding to $NSE > 0.9$ for the MC temperatures at CS 2. The shaded areas contain model bounds for all $NSE > 0.9$ for the MC temperatures at CS 2. The symbols represent observations.

Figure 7. Latin Hypercube sampling simulation results for (a) MC temperatures at CS 2, (b) MC temperatures at CS 3 from parameter sets corresponding to $NSE > 0.9$ for the MC temperatures at CS 3. The shaded areas contain model bounds for all $NSE > 0.9$ for the MC temperatures at CS 3. The symbols represent observations.

Figure 8. Model results using the parameter set corresponding to the smallest value of 1−*NSE* and observations for all zones given a single objective optimization using MC temperatures at CS 2. Model results are shown as solid gray lines. Observed temperature time series are shown as solid black lines in (a) and (b). Observed STS time series are plotted as solid (temperature probe 1, river left) and dashed (temperature probe 1, river right) black lines in (c) and (d). Three observed time series are plotted in (e) and (f) as three different black line types corresponding to 3cm (temperature probe 5, solid line), 9 cm (temperature probe 6, dashed line), and 20 cm (temperature probe 7, dotted line).

Figure 9. Model results using the parameter set corresponding to the smallest value of 1−*NSE* and observations for all zones given a single objective optimization using MC temperatures at CS 3. Model results are shown as solid gray lines. Observed temperature time series are shown as solid black lines in (a) and (b). Observed STS time series are plotted as solid (temperature probe 1, river left) and dashed (temperature probe 1, river right) black lines in (c) and (d). Three observed time series are plotted in (e) and (f) as three different black line types corresponding to 3cm (temperature probe 5, solid line), 9 cm (temperature probe 6, dashed line), and 20 cm (temperature probe 7, dotted line).

Figure 10. Parameter sets associated with last 300 optimization runs for the single objective simulations. This includes parameter sets for the MC temperature optimization at CS 2 for the upper section (a) and lower section (b) and the MC temperature optimization at CS 3 for the (c) upper section and (d) lower section. The darker lines represent the best parameter set for each calibration.

Figure 11. Model results from the "best" parameter set and observations for all zones given a two-objective optimization using MC temperatures at CS 2 and MC temperatures at CS 3. Model results are shown as solid gray lines. Observed temperature time series are shown as solid black lines in (a) and (b). Observed dead zone time series are plotted as solid (temperature probe 1, river left) and dashed (temperature probe 1, river right) black lines in (c) and (d). Three observed time series are plotted in (e) and (f) as three different black line types corresponding to 3cm (temperature probe 5, solid line), 9 cm (temperature probe 6, dashed line), and 20 cm (temperature probe 7, dotted line).

Table 1. Time series data collected and the related parameters.

Time Series Data	Related Parameters
MC Temperature (Probe 2)	B_{tot} , $A_{c,STS}$, α_{STS}, Q_{HTS}, Y_{HTS}, Y_{gr}
STS Temperature (Probe 1, 3)	β, $A_{c,STS}$, α_{STS}
HTS/Sediment Temperatures (Probes 4-6)	Q_{HTS}, Y_{HTS}, Y_{gr}
Cylinder Sediment Temperatures (Probes 8-10)	ρ_{sed}, α_{sed}, $C_{p,sed}$

Table 2. Parameter ranges determined from the Latin Hypercube sampling.

Parameter Description	Parameter Name	Parameter Ranges			
		Lower Section		Upper Section	
		Maximum	Maximum	Minimum	Maximum
Total Channel Width (m)	B_{tot}	15	30	15	30
Manning's Roughness Coefficient	n	0.025	0.06	0.026	0.06
STS Width (% Total Channel Width)	β	5.2	30.0	5.1	29.2
STS CS Area (m^2)	$A_{c,DZ}$	0.51	1.97	0.52	1.98
STS Exchange (m^2 d^{-1})	α_{DZ}	1.95×10^4	8.5×10^4	1.8×10^4	8.5×10^4
HTS Advective Transport Coefficient (m^3 d^{-1})	Q_{HS}	173	410	174	863
Depth HTS (m)	Y_{HS}	0.05	0.99	0.06	1

Table 3. Resulting best parameter sets for all three optimizations.

		Single Objective Optimization Temperature MC CS 2 (Figure 8)		**Single Objective Optimization Temperature MC CS 3 (Figure 9)**		**Two Objective Optimization Temperature MC CS 2 and MC CS 3 (Figure 11)**	
Parameter Description	**Parameter Name**	**Upper Section**	**Lower Section**	**Upper Section**	**Lower Section**	**Upper Section**	**Lower Section**
Total Channel Width (m)	B_{tot}	15	25	15	18	22	16
Manning Roughness	n	0.060	0.042	0.060	0.031	0.060	0.026
Dead-Zone Width (% Total Channel Width)	β	28.9	20.1	25.8	21.9	30	30
Dead-Zone CS Area (m^2)	$A_{c,DZ}$	1.95	1.24	1.96	1.34	2.00	0.51
Dead-Zone Diffusivity (m^2/d)	α_{DZ}	2.51×10^4	5.18×10^4	3.72×10^4	5.62×10^4	6.30×10^4	1.96×10^4
Hyporheic Storage Advective Transport Coefficient (m^3/d)	Q_{HS}	339	257	727	212	863	863
Depth of Hyporheic Storage (m)	Y_{HS}	0.997	0.625	0.60	0.98	0.45	0.99
Depth of Ground Conduction (m)	Y_{gr}	0.53		0.67		1.00	

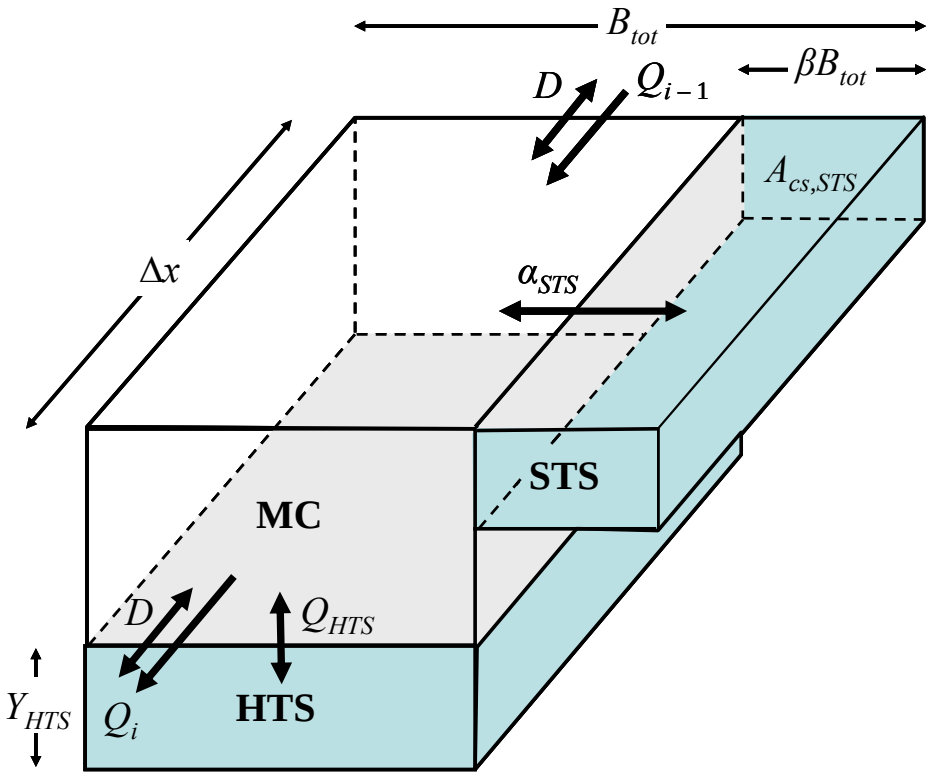

Figure 1. Two-zone model schematic of the connectivity between the main channel (MC), surface transient storage (STS), and subsurface or hyporheic transient storage (HTS).

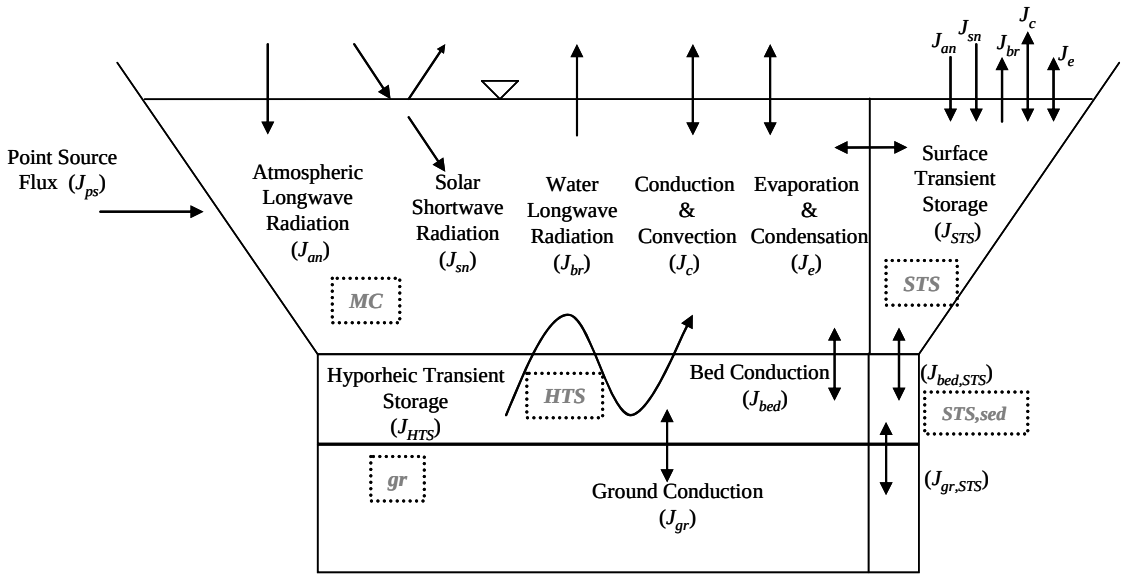

Figure 2. Energy balance components of the two-zone temperature and solute model.

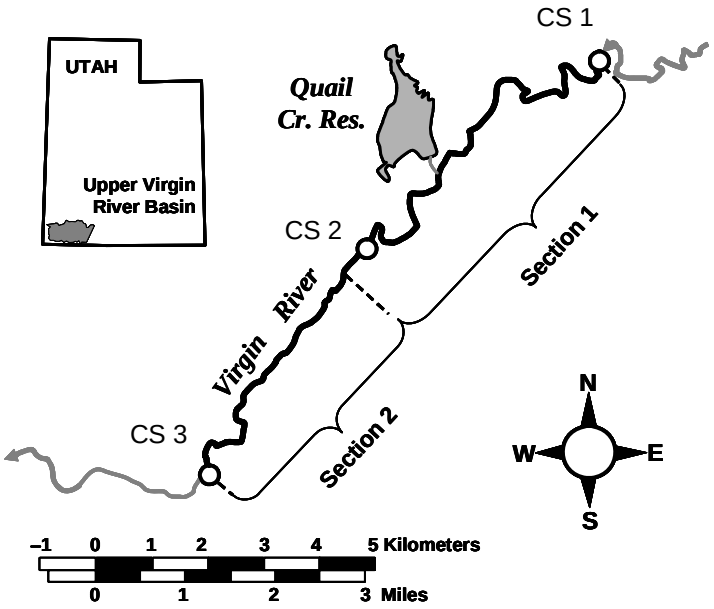

Figure 3. Virgin River study location (taken from Neilson et al. [2009]).

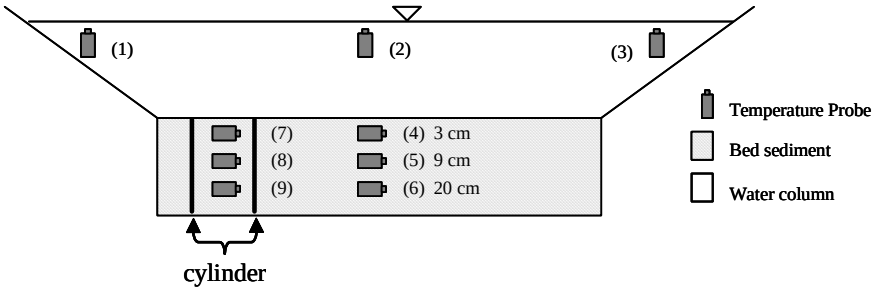

Figure 4. Locations of temperature probes at each of the three locations within the study reach (taken from Neilson et al. [2009]).

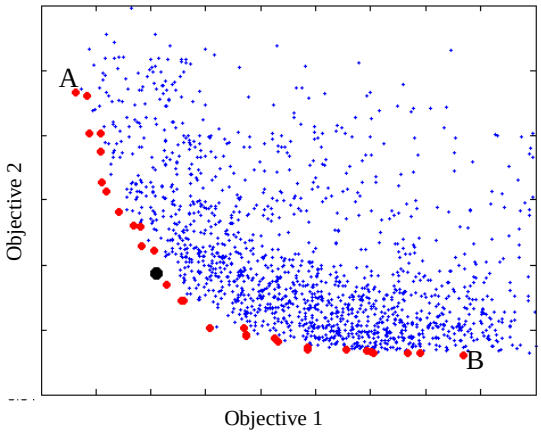

Figure 5. Example objective space emphasizing the Pareto solution set for a two-objective optimization. The larger black dot represents the optimal parameter set given both objectives as the criteria while the other slightly smaller dots represent the rest of the Pareto solution set. The small plus signs represent those that are not part of the Pareto solution set. The points labeled (A) and (B) represent the parameter sets resulting in the minimum value for each objective function.

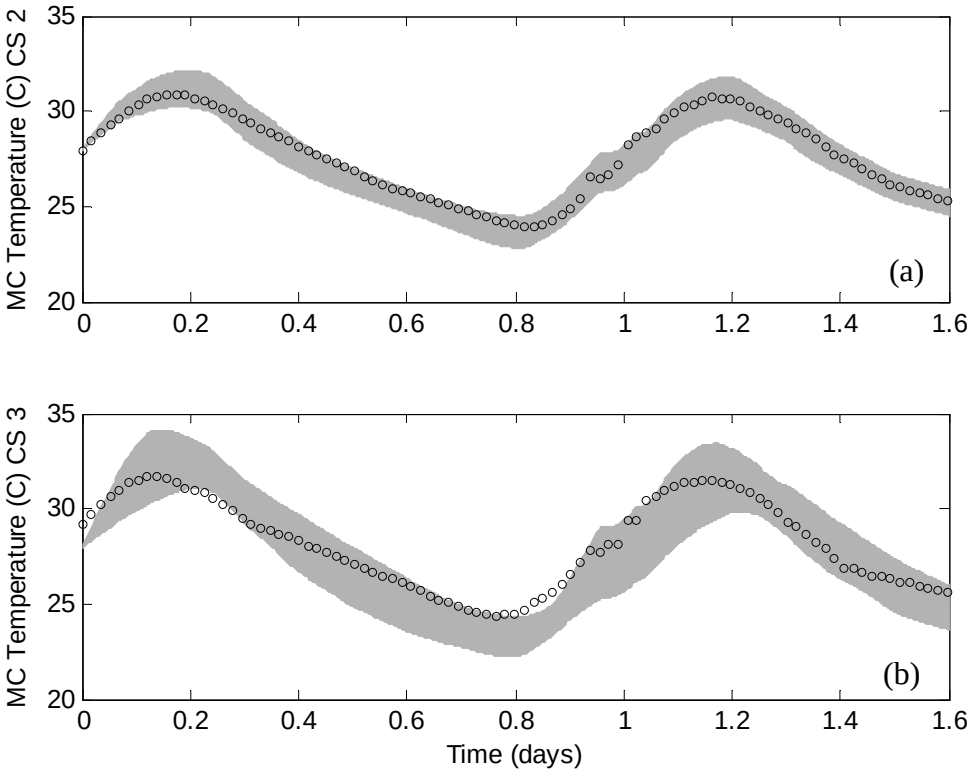

Figure 6. Latin Hypercube sampling simulation results for: (a) MC temperatures at CS 2, (b) MC temperatures at CS 3 from parameter sets corresponding to *NSE* > 0.9 for the MC temperatures at CS 2. The shaded areas contain model bounds for all *NSE* > 0.9 for the MC temperatures at CS 2. The symbols represent observations.

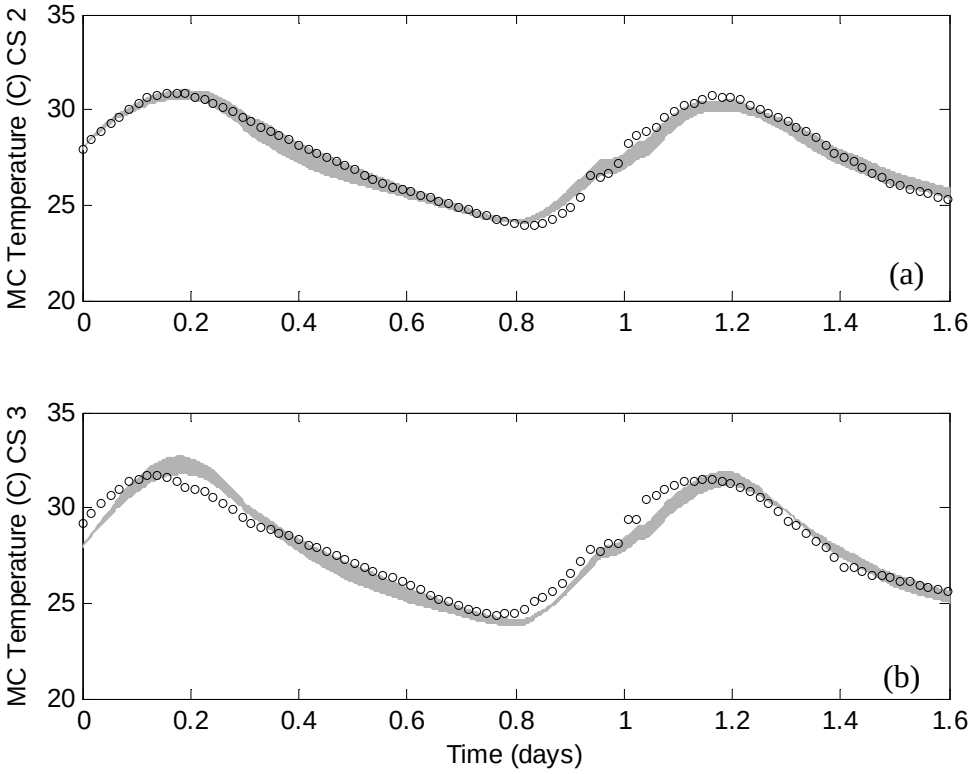

Figure 7. Latin Hypercube sampling simulation results for (a) MC temperatures at CS 2, (b) MC temperatures at CS 3 from parameter sets corresponding to *NSE* > 0.9 for the MC temperatures at CS 3. The shaded areas contain model bounds for all *NSE* > 0.9 for the MC temperatures at CS 3. The symbols represent observations.

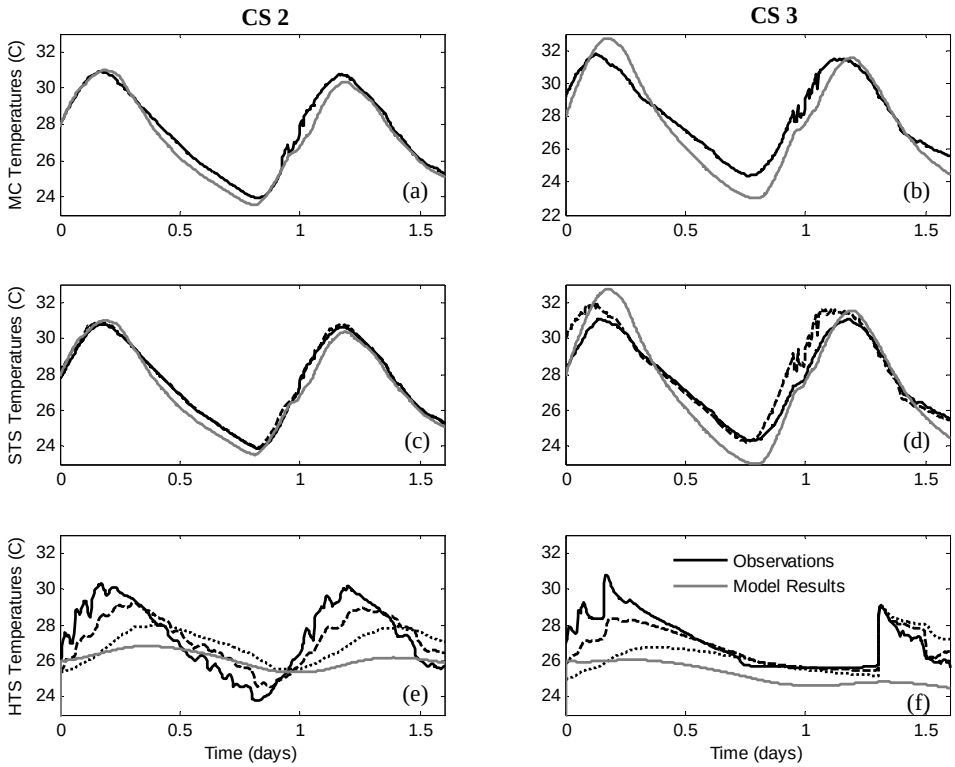

Figure 8. Model results using the parameter set corresponding to the smallest value of 1–*NSE* and observations for all zones given a single objective optimization using MC temperatures at CS 2. Model results are shown as solid gray lines. Observed temperature time series are shown as solid black lines in (a) and (b). Observed STS time series are plotted as solid (temperature probe 1, river left) and dashed (temperature probe 1, river right) black lines in (c) and (d). Three observed time series are plotted in (e) and (f) as three different black line types corresponding to 3cm (temperature probe 5, solid line), 9 cm (temperature probe 6, dashed line), and 20 cm (temperature probe 7, dotted line)

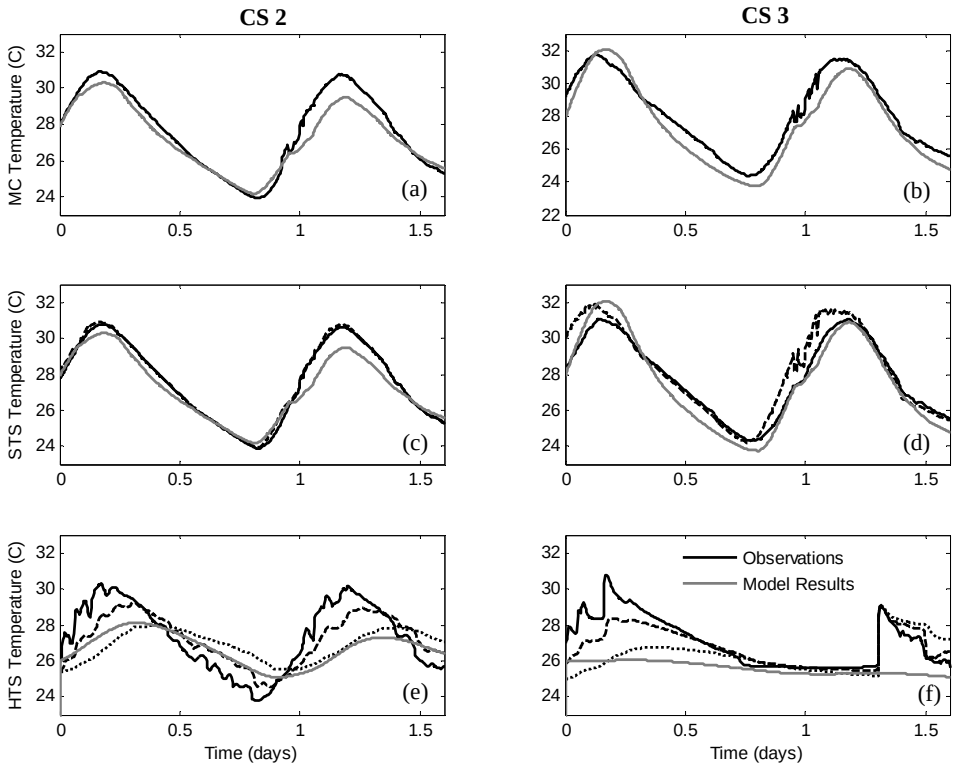

Figure 9. Model results using the parameter set corresponding to the smallest value of 1–*NSE* and observations for all zones given a single objective optimization using MC temperatures at CS 3. Model results are shown as solid gray lines. Observed temperature time series are shown as solid black lines in (a) and (b). Observed STS time series are plotted as solid (temperature probe 1, river left) and dashed (temperature probe 1, river right) black lines in (c) and (d). Three observed time series are plotted in (e) and (f) as three different black line types corresponding to 3cm (temperature probe 5, solid line), 9 cm (temperature probe 6, dashed line), and 20 cm (temperature probe 7, dotted line).

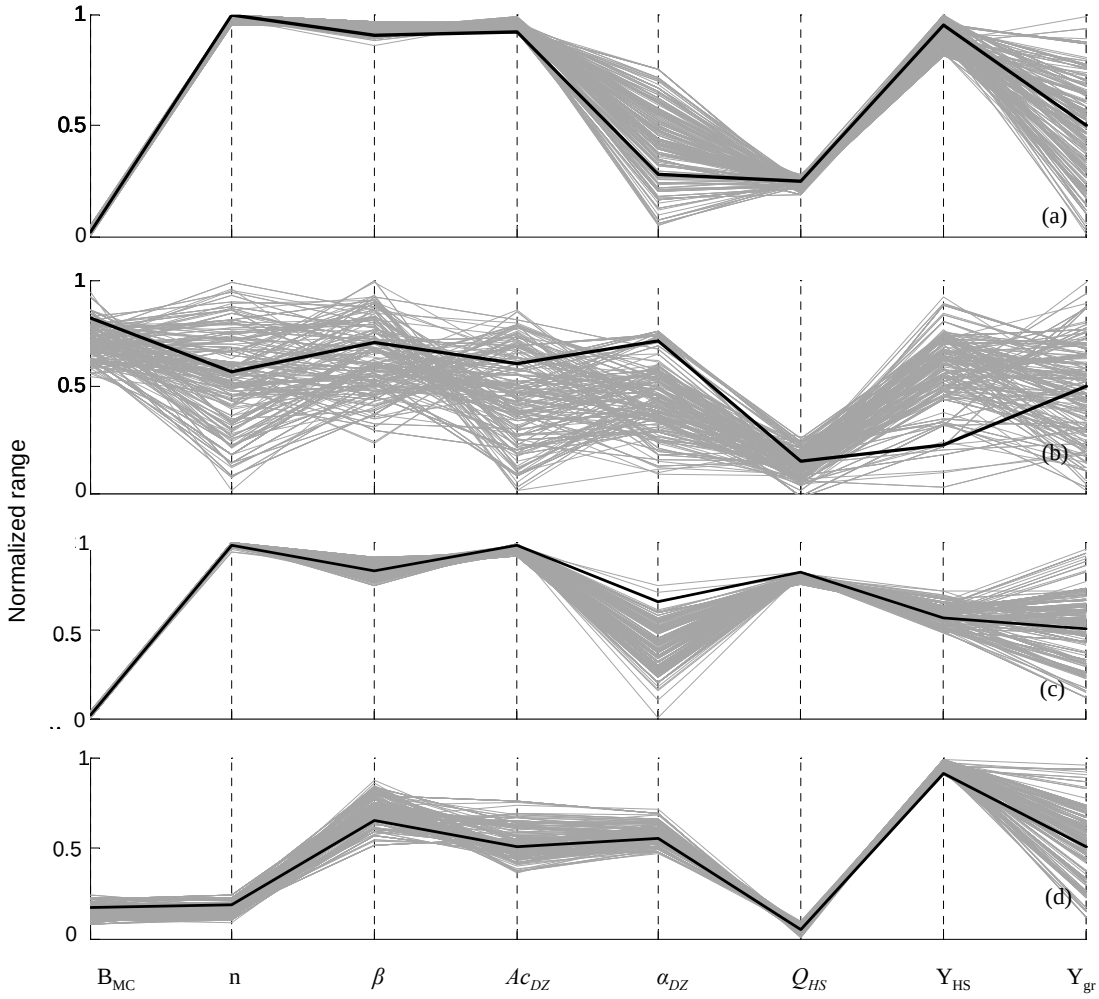

Figure 10. Parameter sets associated with last 300 optimization runs for the single objective simulations. This includes parameter sets for the MC temperature optimization at CS 2 for the upper section (a) and lower section (b) and the MC temperature optimization at CS 3 for the (c) upper section and (d) lower section. The darker lines represent the best parameter set for each calibration.

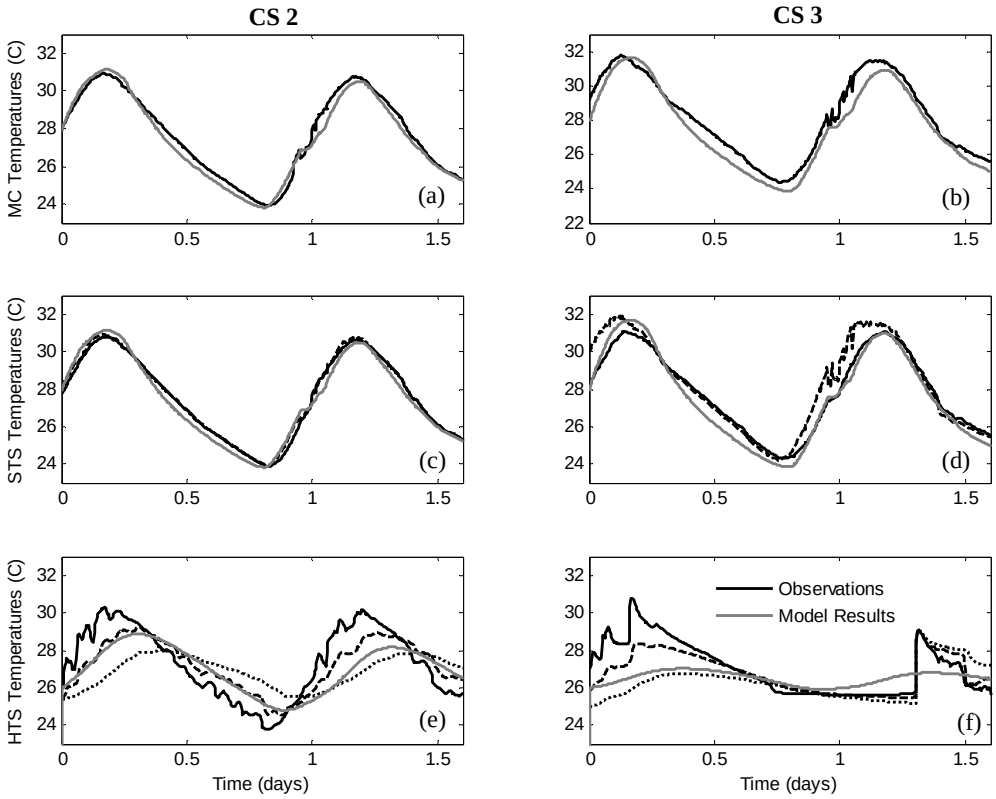

Figure 11. Model results from the "best" parameter set and observations for all zones given a two-objective optimization using MC temperatures at CS 2 and MC temperatures at CS 3. Model results are shown as solid gray lines. Observed temperature time series are shown as solid black lines in (a) and (b). Observed dead zone time series are plotted as solid (temperature probe 1, river left) and dashed (temperature probe 1, river right) black lines in (c) and (d). Three observed time series are plotted in (e) and (f) as three different black line types corresponding to 3cm (temperature probe 5, solid line), 9 cm (temperature probe 6, dashed line), and 20 cm (temperature probe 7, dotted line).